JOURNAL OF PROPULSION AND POWER
Vol. 18, No. 6, November–December 2002

Advanced Performance Modeling of Experimental Laser Lightcraft

Ten-See Wang*
NASA Marshall Space Flight Center, Huntsville, Alabama 35812
Yen-Sen Chen† and Jiwen Liu‡
Engineering Sciences, Inc., Huntsville, Alabama 35802
Leik N. Myrabo§
Rensselaer Polytechnic Institute, Troy, New York 12180
and
Franklin B. Mead Jr.¶
U.S. Air Force Research Laboratory, Edwards Air Force Base, California 93524

A computational plasma aerodynamics model is developed to study the performance of a laser-propelled lightcraft. The computational methodology is based on a time-accurate, multi-dimensional, finite volume, chemically reacting, unstructured grid pressure-based formulation. The underlying physics are modeled using a building-block approach. The physics modeled include nonequilibrium thermodynamics, nonequilibrium air–plasma finite rate kinetics, specular ray tracing, laser beam energy absorption and refraction by plasma, nonequilibrium plasma radiation, and plasma resonance. A series of transient computations are performed at several laser pulse energy levels and the simulated physics are discussed and compared with those of tests and literatures. The computed impulses and coupling coefficients for the lightcraft compared reasonably well with those of tests conducted on a pendulum apparatus.

Nomenclature

A_p, A_m	=	matrix coefficients of transport equations
C	=	coupling coefficient
C_t	=	instantaneous coupling coefficient
$C_{v,v}$	=	constant volume specific heat for vibrational energy
c	=	speed of light in a vacuum
D	=	species diffusivity
E	=	laser pulse energy
e_v	=	vibrational energy
e_v^{eq}	=	equilibrium vibrational energy
$\boldsymbol{F}$	=	flux vector
$F_{i,j}$	=	convection and diffusion fluxes through the interface between cells i and j
H	=	total enthalpy
I	=	intensity, number of quantum levels, or impulse
I_t	=	instantaneous impulse
j	=	emission coefficient
K	=	transfer constant between quantum levels
k_b	=	Boltzmann's constant
k_c	=	Coulomb constant
$k(i)$	=	a list of faces of cell i
k_v	=	thermal conductivity
M	=	molecular weight or Mach number
m_e	=	electron mass
N	=	total quantum level population
N_i	=	quantum level
n	=	refraction index
$\boldsymbol{n}$	=	unit normal vector in the outward direction
n_e	=	electron number density
Pr	=	Prantdl number
p	=	gas static pressure
p_e	=	electron partial pressure
Q_c	=	nonelastic collision energy transfer
Q_{re}	=	net electron radiative heat source
Q_{rg}	=	net heavy gas radiative heat source
Q_v	=	vibrational–translational energy transfer
q_e	=	electron charge
$\boldsymbol{r}$	=	position vector
S	=	source terms
T	=	gas temperature, K
T_e	=	electron temperature, K
T_t	=	translational temperature, K
T_v	=	vibrational temperature, K
t	=	time, s
u_i	=	velocity components
V	=	velocity magnitude
x_i	=	Cartesian coordinates
α	=	species mass fraction
Γ	=	control surface
$\Delta\Gamma_j$	=	cell-face area
ε_0	=	permittivity
θ	=	refractive angle
κ_l	=	laser absorption coefficient
λ_e	=	electron species thermal conductivity
λ_l	=	laser wavelength
μ	=	viscosity
ρ	=	density
τ_{ij}	=	shear stress tensor
τ_{LT}	=	vibrational–translational relaxation timescale

Presented as Paper 2001-0648 at the AIAA 39th Aerospace Sciences Meeting and Exhibit, Reno, NV, 8–11 January 2001; received 19 June 2001; revision received 18 July 2002; accepted for publication 18 July 2002.

*Staff, Applied Fluid Dynamics Group, Space Transportation Directorate. Senior Member AIAA.
†President. Member AIAA.
‡Senior Research Engineer. Senior Member AIAA.
§Associate Professor, Aerospace Engineering Department. Senior Member AIAA.
¶Senior Scientist, Propulsion Directorate. Member AIAA.

$\langle\tau_s\rangle$ = vibrational–translational energy relaxation time for molecular species, s
ϕ = dependent variable
Ω = control volume domain
$\dot{\omega}_i$ = chemical reaction source term
ω_p = plasma frequency

Introduction

BEAMED energy propulsion was first promoted by Kantrowitz.[1] Since then, propulsion systems supported by a laser-sustained plasma have been the subject of many studies.[2–6] The main advantage gained by laser propulsion is the low-weight system derived from decoupling the energy source from the vehicle and high specific impulse resulting in low fuel consumption. The first ground and flight tests of a ground-based laser-propelled vehicle were reported in 1998,[7] in which active tracking and beam control were demonstrated to 122 m on a horizontal wire and spin-stabilized free flights in the laboratory were acheived to an altitude of 4 m. Six months later, the spin-stabilized vertical free flights outdoors reached 30 m (Ref. 8). These results were accomplished with axisymmetric vehicles that are of a special design, in which a nosecone-shaped forebody, an annular shroud, and a parabolic afterbody are the only major components. A vehicle of such design is called the laser lightcraft in this study. A hybrid computational grid with component definition is shown in Fig. 1. The parabolic afterbody surface serves both as an aerospike nozzle and also as the main receiving optic, whereas the annular shroud surrounds the ring focus of the parabolic optic. The laser lightcraft operates in both the rocket and airbreathing modes. When operating in an airbreathing mode, the specific impulse is infinity because no fuel is consumed. These successful tests[7,8] demonstrated the concept, but the feasibility of launching small payload with a laser lightcraft requires more detailed study.

When the focused beam energy strikes the shroud of a laser lightcraft, free electrons form to invoke inverse Bremsstrahlung (IB) absorption of laser energy, and the optical breakdown ensues. To achieve maximum intensity and to avoid undue plasma resonance, repetitive short pulses are used. As such, repetitive pulsed detonation waves (PDW) are generated to propel the vehicle, hence, the laser lightcraft engine is also known as a PDW engine. It can be seen that the underlying physics involved, such as IB and PDW, are so complicated that a simple system model is not capable of describing the phenomena, let alone predicting the thrust performance and the associated flow and thermal environments necessary for designing for the structure integrity. A detailed computational plasma aerodynamics model is, therefore, needed for the design and scaling of future laser lightcraft.

From May to July 1999, performance data in the form of coupling coefficients were taken in a series of indoor tests for the Model 200 series vehicles. Armed with these data for comparison purposes, a computational plasma aerodynamics methodology is developed as a first attempt to predicting the thrust performance of a PDW engine propelled laser lightcraft.

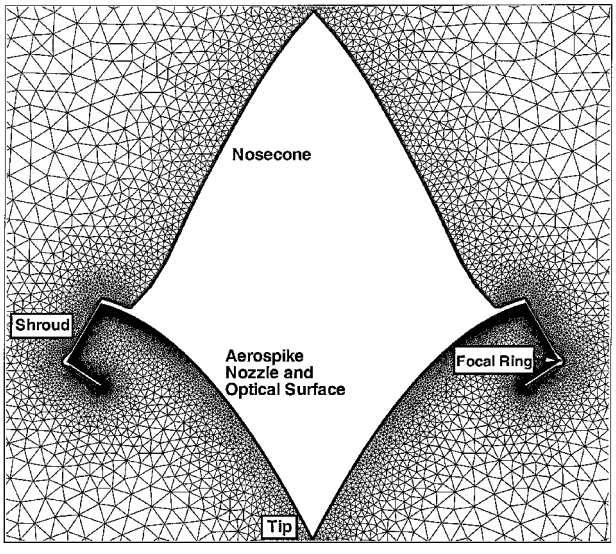

Fig. 1 Hybrid computational grid with component definition for Laser Lightcraft Model 200-3/4.

Computational Plasma Aerodynamics Development

Several attempts have been made to model the physics inside continuous wave devices analytically or computationally. For example, an early effort by Raizer[9] assumed constant-pressure one-dimensional flow in air with heat addition by a laser. Thermal conduction was considered dominant, and the radiation loss from the plasma was ignored. Kemp and Root[10] later extended this one-dimensional analysis to hydrogen and to include thermal radiation. Molvik et al.[5] extended this problem to a two-dimensional structured-grid hydrogen flow and implemented real ray tracing, but ignored thermal radiation. Jeng and Keefer[4] performed a similar analysis and added thermal radiation. Myrabo et al.[6] later simulated the radiative-gasdynamics processes in optical discharges maintained in a subsonic De Laval nozzle. In this paper, a multidimensional unstructured-grid computational plasma aerodynamics methodology is developed for pulsed wave devices, with emphases on nonequilibrium effects and laser-induced physics such as laser–plasma interactions. Realistic laser absorption coefficients are used. The governing equations will be described first, with the auxiliary equations that compute the nonequilibrium and laser-induced physics to follow.

Governing Equations

To describe the plasma aerodynamics involved in laser-propelled propulsion properly, the time-varying transport equations of continuity, species continuity, momentum, global energy (total enthalpy), and electron energy are formulated and written in a Cartesian tensor form:

$$\frac{\partial \rho}{\partial t} + \frac{\partial}{\partial x_j}(\rho u_j) = 0$$

$$\frac{\partial \rho\alpha_i}{\partial t} + \frac{\partial}{\partial x_j}(\rho u_j \alpha_j) = \frac{\partial}{\partial x_j}\left[(\rho D)\frac{\partial \alpha_i}{\partial x_j}\right] + \omega_i$$

$$\frac{\partial \rho u_i}{\partial t} + \frac{\partial}{\partial x_j}(\rho u_j u_i) = -\frac{\partial p}{\partial x_i} + \frac{\partial \tau_{ij}}{\partial x_j}$$

$$\frac{\partial \rho H}{\partial t} + \frac{\partial}{\partial x_j}(\rho u_j H) = \frac{\partial p}{\partial t} + Q_{rg} + Q_c + Q_v + \frac{\partial}{\partial x_j}\left(\frac{\mu}{Pr}\nabla H\right) + \frac{\partial}{\partial x_j}\left[\left(1 - \frac{\mu}{Pr}\right)\nabla\left(\frac{V^2}{2}\right)\right]$$

$$\frac{\partial}{\partial t}\left(\frac{2}{3}k_b n_e T_e\right) + \frac{\partial}{\partial x_j}\left(\frac{2}{3}k_b n_e T_e u_j\right) = \frac{\partial}{\partial x_j}\left(\lambda_e \frac{\partial T_e}{\partial x_j}\right) + Q_{re} - Q_c$$

where the shear stress τ_{ij} can be expressed as

$$\tau_{ij} = \mu\left(\frac{\partial u_i}{\partial x_j} + \frac{\partial u_j}{\partial x_i} - \frac{2}{3}\frac{\partial u_k}{\partial x_k}\delta_{ij}\right)$$

The beam energy absorption, beam energy transfer, and plasma radiation are invoked through the source terms of the global energy and the electron energy equations, whereas the air plasma species are generated and consumed through the source terms of the species continuity equations. Air plasma species include the following atomic, molecular, and ionized species: O, N, NO, N^+, O^+, NO^+, N_2, O_2, N_2^+, O_2^+, and e^-. Transport and thermodynamic properties of these species are obtained from Gupta et al.[11] and Gordon and Mcbride,[12] respectively. The nonelastic energy transfer is formulated after Nagulapally et al.[13]

Numerical Scheme

The cell-centered scheme is employed to allow the volume surfaces to be represented by the grid cell surfaces. The transport equations can be written in integral form as

$$\frac{\partial}{\partial t}\int_{\Omega}\rho\phi\,\mathrm{d}\Omega+\oint_{\Gamma}\boldsymbol{F}\cdot\boldsymbol{n}\,\mathrm{d}\Gamma=\oint_{\Omega}S_{\phi}\,\mathrm{d}\Omega$$

The flux function $\boldsymbol{F}$ contains the inviscid and the viscous flux vectors,

$$\boldsymbol{F}=\rho\boldsymbol{V}\phi-\mu_{\phi}\nabla\phi$$

Let us consider a control volume interface e between control volumes E and P, with a normal vector n. Also, $\phi_E-\phi_P\approx\overline{\nabla\phi}_e\cdot(\boldsymbol{r}_E-\boldsymbol{r}_P)$, where $\overline{\nabla\phi}_e$ is interpolated from the neighbor cells E and P. For the face e between control volumes P and E, the diffusive flux can be approximated as

$$(\nabla\phi\cdot\boldsymbol{n})_e\approx\frac{\phi_E-\phi_P}{|\boldsymbol{r}_E-\boldsymbol{r}_P|}+\overline{\nabla\phi}_e\cdot\left(\boldsymbol{n}-\frac{\boldsymbol{r}_E-\boldsymbol{r}_P}{|\boldsymbol{r}_E-\boldsymbol{r}_P|}\right)$$

The finite volume formulation of flux integral can be evaluated by the summation of the flux vectors over each face,

$$\oint_{\Gamma}\boldsymbol{F}\cdot\boldsymbol{n}\,\mathrm{d}\Gamma=\sum_{j=k(i)}F_{i,j}\Delta\Gamma_j$$

The convective flux is evaluated through the upwind-cell quantity by a linear reconstruction procedure to achieve second-order accuracy, $\phi_e=\phi_u+\phi_e\nabla\phi_u\cdot(\boldsymbol{r}_e-\boldsymbol{r}_u)$, where the subscript u represents the upwind cell and ψ_e is a limiter used to ensure that the reconstruction does not introduce local extrema. The limiter proposed by Barth[14] is used here. Defining $\phi_{\max}=\max(\phi_u,\phi_j)$ and $\phi_{\min}=\min(\phi_u,\phi_j)$ (and assuming ϕ_e^0 is computed with $\psi_e=1$) the scalar ψ_e associated with the gradient at cell u due to edge e is

$$\psi_e=\begin{cases}\min\left(1,\dfrac{\phi_{\max}-\phi_u}{\phi_e^0-\phi_u}\right) & \text{if} \quad \phi_e^0-\phi>0\\ \min\left(1,\dfrac{\phi_{\min}-\phi_u}{\phi_e^0-\phi_u}\right) & \text{if} \quad \phi_e^0-\phi<0\\ 1 & \text{if} \quad \phi_e^0-\phi=0\end{cases}$$

Solution Procedures

A general implicit discretized time-marching scheme for the transport equations can be written as

$$\left(\frac{\rho^n}{\Delta t}+A_p\right)\phi_p^{n+1}=\sum_{m=1}^{\mathrm{NB}}A_m\phi_m^{n+1}+\frac{(\rho\phi_p)^n}{\Delta t}+S_{\phi}$$

where NB means the neighbor cells of cell P. The high-order differencing term and cross-diffusion term are treated using known quantities and retained in the source term and updated explicitly. The second term of the right-hand side (RHS) is a perturbation that comes from the RHS. A predictor and corrector solution algorithm is employed to provide coupling of the governing equations. A second-order central-difference scheme is employed to discretize the diffusion fluxes and source terms of the governing equations. For the convective terms, a second-order total variation diminishing difference scheme is used in this effort. To enhance the temporal accuracy, a second-order backward difference scheme is employed to discretize the temporal terms. The discretized finite volume equations form a set of linear algebraic equations that comprise a nonsymmetric matrix system with arbitrary sparsity patterns. The Bi-CGSTAB[15] and GMRES[16] (for pressure–velocity coupling) matrix solvers are used to solve the linear algebraic equations efficiently.

Auxiliary Equations

Thermal Nonequilibrium Energy Equations

For high-temperature flows, the thermal nonequilibrium state may be important. In Landau and Teller's derivation,[17] a master equation is employed to describe the evolution of the population of quantum level N_i. This master equation is written as

$$\frac{\mathrm{d}N_i}{\mathrm{d}t}=N\sum_{j=0}^{I_{\max}}K_{j\Rightarrow i}N_j-N\sum_{j=0}^{I_{\max}}K_{i\Rightarrow j}N_i,\qquad i=0,1,2,\ldots,I_{\max}$$

Results from the quantum mechanical solution of the harmonic oscillator are used to relate the various quantum transition rates to one another, and then the master equation may be summed over all quantum states to obtain the Landau–Teller[17] equation:

$$\frac{\mathrm{D}\rho e_v}{\mathrm{D}t}=\frac{\partial}{\partial x_i}\left(k_v\frac{\partial T_v}{\partial x_i}\right)+\rho\frac{e_v^{\mathrm{eq}}(T_t)-e_v}{\tau_{\mathrm{LT}}}$$

An empirical expression[18] is used to model the Landau–Teller[17] relaxation timescale

$$\tau_{\mathrm{LT}}=\frac{\sum_{s=\mathrm{mol}}\rho_s/M_s}{\sum_{s=\mathrm{mol}}\rho_s/M_s\langle\tau_s\rangle}$$

where subscript s represents the participating species. (Only diatomic species are involved.) To solve this vibrational energy equation, the source term Q_v is simplified by making the following approximations, following Gnoffo et al.[18]:

$$\rho\left[e_v^{\mathrm{eq}}(T_t)-e_v\right]\Big/\tau_{\mathrm{LT}}=\rho[C_{v,v}(T-T_v)/\tau_{\mathrm{LT}}]$$

The vibrational temperature is used to influence the reaction rates of chemical reactions by assuming that the rate coefficients for dissociation are functions of the geometrical mean temperature between T and T_v (Ref. 19).

Nonequilibrium Air Chemistry

A point-implicit (operator splitting) method is employed to solve the chemistry system. For the breakdown of air, Park's multitemperature air chemistry[19] is the baseline in this study. This mechanism is composed of the dissociation, NO exchange, associative ionization, charge exchange, electron-impact ionization, and radiative recombination reactions. With this mechanism, electrons are produced first by the associative ionization process, and more electrons are produced by the electron-impact reactions. Because the number of electrons doubles in each such event, electron density increases exponentially, in the form of an avalanche.[19] This mechanism, thus, provides the initial electron density for ignition and produces the avalanche of electrons necessary for the subsequent optical breakdown. The reaction rates were validated[19] with experiments of post-shock temperatures ranging from 20,000 to 60,000 K.

Plasma Initiation

Understanding the mechanisms responsible for plasma initiation (ignition) has been the subject of ongoing research. A spark gap, an extremely intense pulse of laser energy striking the focal point, seeded molecules, or particles, or a retractable tungsten target placed at the focal point,[20] have been used as sources of free electrons for initiation.[2] It has also been shown that plasma can be ignited quite easily off of metal surfaces.[2] Likewise, in numerical modeling, initial free electrons are required for plasma ignition. This means determining an initial electron density or a threshold breakdown intensity. For example, Mertogul[20] described an initial electron density that is necessary for modeling the ignition of a hydrogen plasma initiated with a retractable tungsten wire. In this study, a threshold breakdown intensity approach is devised in anticipation of a different threshold breakdown intensity possibly being encountered for differing surface material, target approach, and laser power. The advantage of this approach is that the threshold breakdown intensity can either be calibrated or measured. For example, the effect of seeds on laser breakdown intensity has been reported.[2] In this study, this approach is accomplished by performing parametric studies on plasma initiation with spark time, spark region, and spark power. A spark provides a fixed amount of energy (spark energy) in a region

(spark region) centered around the focal point for a fixed amount of time (spark time). When the strength of a spark reaches a threshold, or the threshold breakdown intensity is satisfied, a laser-supported combustion or detonation is initiated.

This means that enough seed electrons are produced through the likes of associative ionization reactions such that the subsequent optical breakdown (ignition) is possible. It is found that an ignition is sustainable when the energy absorbed by the plasma reaches 15% of that irradiated. Spark times computed based on that criterion range from 1.05 to 2.75 μs. As expected, lower laser pulse energies require longer spark times for ignition. It is also reasonable to assume that the plasma initiates in a (spark) region enclosed by the two outer laser rays and an arc with an origin at the focal point (in a two-dimensional sense), and the (spark) radius of that region is determined empirically as 1 mm. In actuality, the spark region is a torus generated by a pie-shaped cross section rotated about the vehicle axis. Finally, the spark power is also empirically determined as 25% of that of the incident laser.

Laser Radiation

Geometric optics are used to simulate the local intensity of the laser beam, which is split into a number of individual rays. In the presence of absorption, the local intensity of each ray follows the Beer's law:

$$\frac{\mathrm{d}I_i}{\mathrm{d}s_i} = -\kappa_l I_i$$

A ray may change its propagating direction due to the inhomogeneous refractive index within the hot plasma. The index of refraction is taken from Edwards and Fleck[21]:

$$n = \left[1 - \left(\frac{n_e \lambda_l q_e k_c}{m_e c^2 \pi}\right)\right]^{\frac{1}{2}}$$

The refracted angle is associated with the refractive index through the Snell's law (see Ref. 22):

$$n_1 \sin\theta_1 = n_2 \sin\theta_2$$

where n_1 and n_2 represent the refractive indexes for two different control volumes, and θ_1 and θ_2 are the incident and refracted directions with respect to the normal direction of the interface between two volumes.

The electron is the only plasma species that absorbs the laser energy. The absorption coefficient of the CO_2 laser radiation, corrected for stimulated emission in the single ionization range, is approximated by the formula[23]:

$$\kappa_{l\mathrm{CO}_2} = \frac{5.72 p_e^2 \ln\left[27(T/10^4)^{\frac{4}{3}} p_e^{-\frac{1}{3}}\right]}{(T/10^4)^{\frac{7}{2}}}$$

Because the computed peak electron and heavy gas temperatures are in the range of 100,000–200,000 K, well above the threshold temperature for double ionization,[23] a simple averaged ion charge method is used to correct the preceding equation for the effect of multiple ionization. This is accomplished by multiplying the single ionization absorption coefficient with a correction factor, which is a function of the square of an averaged ion charge. For air plasma, this averaged ion charge is tabulated as a function of temperature and electron number density.[24]

Nonequilibrium Plasma Radiation

Treatment of radiative heat transfer of the plasma is different from that of the laser and the solution of the radiative transfer equation (RTE) is required. When transients are neglected, and a nonscattering medium is assumed, the complete RTE becomes

$$\frac{\mathrm{d}I(s,\boldsymbol{\Omega})}{\mathrm{d}s} + \kappa I(s,\boldsymbol{\Omega}) = j(s)$$

In equilibrium gases, the electronic energy-level populations are determined as a function of a uniquely defined equilibrium temperature according to a Boltzmann distribution. Also κ and j are related according to Kirchhoff's law as $j(s) = \kappa I^b(s)$, where $I^b(s)$ is the blackbody intensity determined by Planck's function. In nonequilibrium flows, however, all of these simple relations no longer apply, whereas the nonequilibrium absorption and emission coefficients must be determined by nonequilibrium populations of each energy level and by the transitions among various energy levels.

All air plasma species contribute to the nonequilibrium radiative heat transfer. To determine κ and j for these species, the following four radiative transitions must be taken into account: atomic line transitions, atomic bound–free transitions, atomic free–free transitions, and molecular transitions. The LORAN[25] code provides detailed information on these transitions and is used to calculate the air plasma radiative properties for its relatively small database.

With the determination of κ and j, the RTE can be solved by either a deterministic or a stochastic approach. Unlike the computational plasma aerodynamics governing equations, RTE is an integral differential equation and numerical treatment is, thus, different from those for differential equations. Currently, there are several methods available for solving nonequilibrium radiative heat transfer, which include the Monte Carlo method,[26] P-1 method,[27] quadromoment method,[28] discrete ordinates method (DOM),[29] discrete transfer method (DTM),[30] etc. The Monte Carlo method is adequate, but too time consuming for practical applications. The P-1 and quadromoment methods are only adequate for an optically thick medium. The DOM and DTM are mathematically simple and can provide adequate results for all optical ranges if the discrete direction number is reasonably large. Thus, the DOM and DTM are suitable for modeling radiation with a participating medium. For the laser lightcraft application, the high-temperature region where nonequilibrium radiation is prominent is usually small compare to the entire computational domain. If the DOM is applied, RTE must be solved for the entire flow domain, thus, much of the computational time is wasted in regions where radiation is not important. On the other hand, with the DTM, RTE can be solved in a designated area. The more efficient DTM is selected to solve the RTE.

Plasma Resonance

The plasma frequency is described as a property of a space-charge-neutral plasma[31,32] by which the motion of the electrons in specific electrostatic oscillations is characterized. The plasma frequency ω_p of the electrostatic oscillation of the electrons is defined as[31]

$$\omega_p^2 = n_e q_e^2 / m_e \varepsilon_0$$

Note that plasma frequency is a function only of the electron density. The electrostatic oscillations cause a resonance of the plasma to incident (laser) electromagnetic waves of the same frequency, which are then totally reflected.[32] A critical electron density above which the laser beam is totally reflected can then be obtained by equating the angular frequency of the incident laser with that of the plasma.

Experimental Setup

The 10-kW pulsed laser vulnerability test system (PLVTS) CO_2 laser at the High Energy Laser System Test Facility, White Sands Missle Range, New Mexico, was used to provide the beam energy for laser lightcraft impulse experiments. The CO_2 laser delivered up to 800-J single pulses. The laser pulse energy was measured with a calorimeter, and the uncertainty of the delivered energy was estimated to be ± 10 J. Several variations of the basic laser lightcraft design (Model 200 series), similar to those described in Refs. 7 and 8, were examined, and the test results of the 6061-T6 all aluminum Model 200-3/4 vehicle and Model A vehicle[7] are chosen for this study. The pulse width was 18 μs for Model 200-3/4 tests and 30 μs for Model A tests. The impulse measurements were conducted with a pendulum apparatus. This technique employed a velocimeter coil, which was used in previous work to determine the impulse imparted to a flat plate using the PHAROS III laser at the U.S. Naval

Research Laboratory.[33] The laser lightcraft was suspended and suitably weighed before being subjected to a single pulse of energy from the PLVTS laser. The uncertainty in the impulse measurement is estimated to be 1% or better. Details of the laser, measurement technique, and pendulum apparatus can be found in Refs. 7 and 8.

Computational Grid Generation

Figure 1 shows the layout of a computational grid (for Model 200-3/4). As described earlier, the laser lightcraft consists of a forebody (nose), an annular shroud, and a PDW engine (parabolic optic). Only one-half of the grid shown in Fig. 1 is actually solved due to the axisymmetric formulation. A single-zone, 14,441-point hybrid grid was generated using a grid generation code called GRIDGEN.[34] Quadrilateral elements are used for the wall boundary layer, and triangular elements are used for the rest of the domain. High grid density is used in the inner shroud region and along the optical surface for capturing the optical breakdown and pulsed detonation wave propagation processes.

Results and Discussion

A series of transient computations have been performed for average laser pulse energies of 75, 100, 150, 200, 300, and 400 J for Model 200-3/4 and 400, 600, and 800 J for Model A, simulating propulsion physics encountered by those experimental lightcraft during impulse measurements using a single pulse of laser energy. Figure 2 shows the computed electron temperature contours and laser beam traces at elapsed times of 10, 18, and 100 μs, respectively, pulsed by 400 J of laser energy. It can be seen that the laser beam reflects specularly on the optical surface and focuses onto a focal point on the shroud where the breakdown of air occurs. The specular reflection on the parabolic surface is done analytically by making the surface points a part of a parabola through the boundary treatment. There are 11 laser rays plotted for clarity, whereas 200 rays are actually used in the computation. Note that the rays are allowed to bend as the index of refraction varies with the expanding plasma.

It is probably best to recount the phenomenon of an optical detonation wave, which is a detonation wave generated by the optical breakdown of a medium with an incident laser beam, at this moment. This phenomenon was put forward by Raizer and Tybulewicz[23] in detail in their book. Essentially, a strong shock wave is generated in the region where the laser radiation that produces the plasma is absorbed and heat is deposited very rapidly. This shock wave travels through the medium, heating and ionizing it such that the medium becomes capable of absorbing more laser radiation. The laser energy is deposited in successive layers of a medium adjoining the front of the shock wave subjected to the laser radiation. These layers themselves, thus, become energy sources that maintain the shock wave. Hence, the shock wave moves along the optical channel in the opposite direction to the laser beam. Thus, during the initial stages, the shock wave is maintained by the laser beam and does not decay.

The electron temperature contours in Fig. 2 also describe the growth of the plasma front. The "protrusion" of the plasma front at 10 and 18 μs indicates that the plasma front (and the shock wave) is propagating up the beam, a result of successive heating and ionizing of the medium (air) such that the medium becomes capable of absorbing more laser energy and propagates further. This is an indication of the computed optical breakdown phenomenon qualitatively agreeing with that given by Raizer and Tybulewicz.[23] The spreading of the waves outside the optical channel results in gradual attenuation because of the lack of energy support. At 100 μs, when the laser is long turned off, the optical breakdown is not being maintained by the laser irradiation and the electron temperature decreases, as do other plasma properties such as ions, neutrals, and electron number densities. The shock wave moves out of the shroud region rapidly, leaving the plasma cloud behind and trailing in a slow, vortical motion. Figure 3 shows time slices of the electron number density contours computed at same elapsed times as those in Fig. 2. Again, the snapshots at 10 and 18 μs exhibit the growth of the plasma front inside the optical channel. At 100 μs, the electron number density contours show a maximum at the tip. This is caused by an increase of pressure at the tip where the shock wave converges.

Figure 4 shows the computed maximum shock Mach number, pressure, and electron number density histories. This is achieved by searching for the maximum value throughout the entire computational domain and by recording it at every time integration step. As shown in Fig. 4, there are three distinct peaks in these curves, signifying three time events: the ignition of the plasma, the impingement

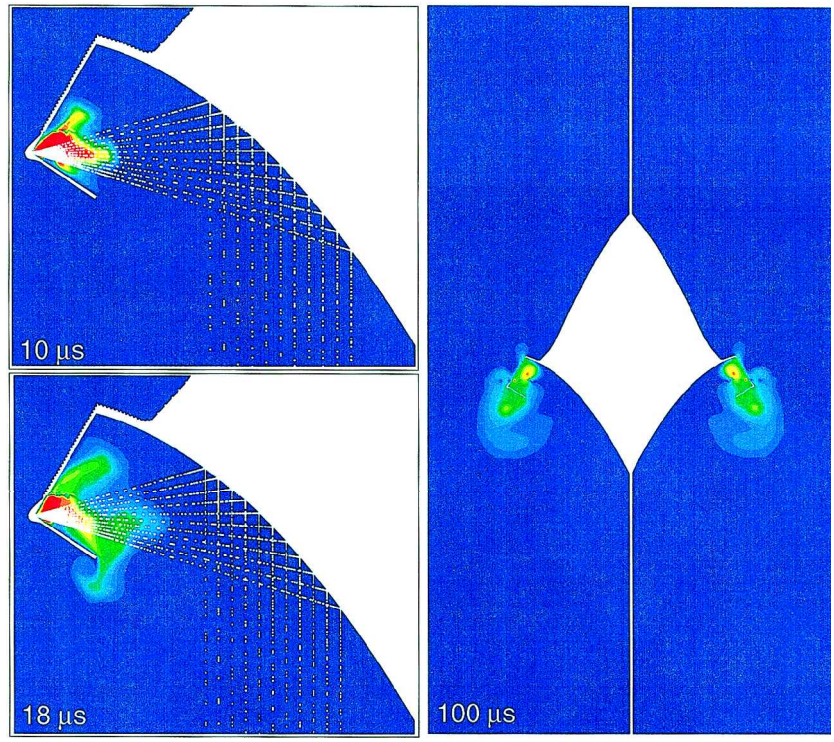

Fig. 2 Computed electron temperature contours and laser ray traces for Model 200-3/4 pulsed by 400-J laser energy; contours color scale: 10 μs, 7600–109,640, maximum 195,575; 18 μs, 8900–129,300, maximum 137,910; and 100 μs, 890–9190, maximum 9780.

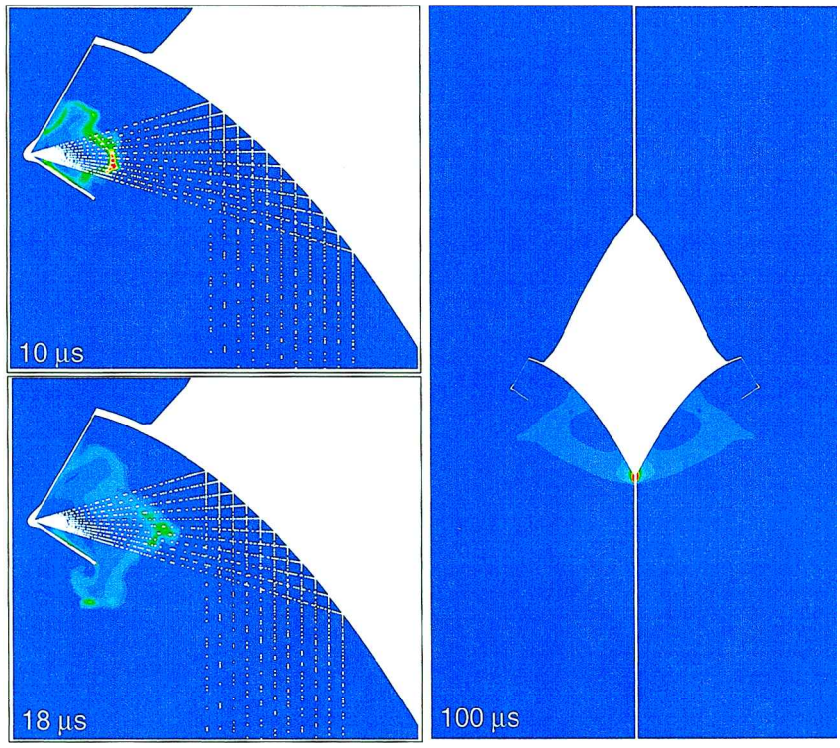

Fig. 3 Computed electron number density contours for Model 200-3/4 pulsed by 400-J laser energy; contours color scale: 10 μs, 1–1.8 × 10^{24}; 18 μs, 1–2.4 × 10^{24}; and 100 μs, 1–5 × 10^{22}.

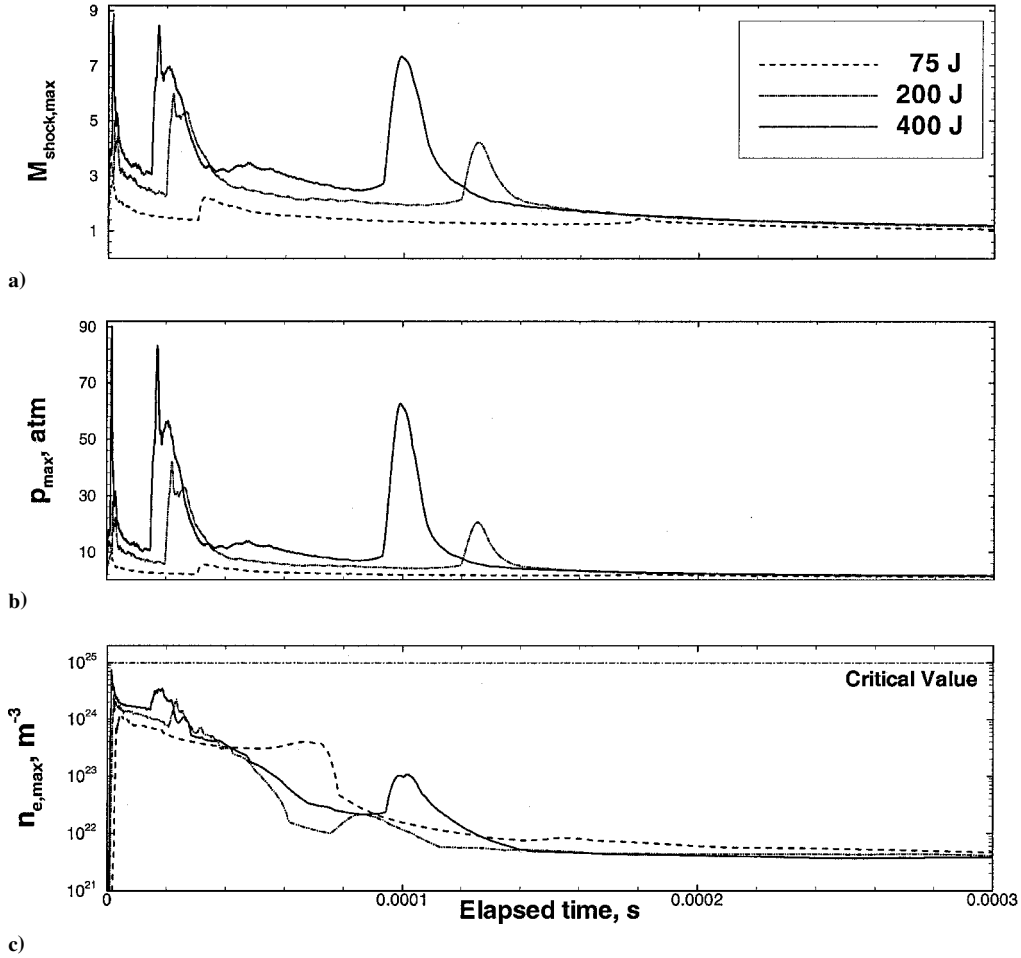

Fig. 4 Computed a) maximum shock Mach number, b) pressure, and c) electron number density histories for Model 200-3/4.

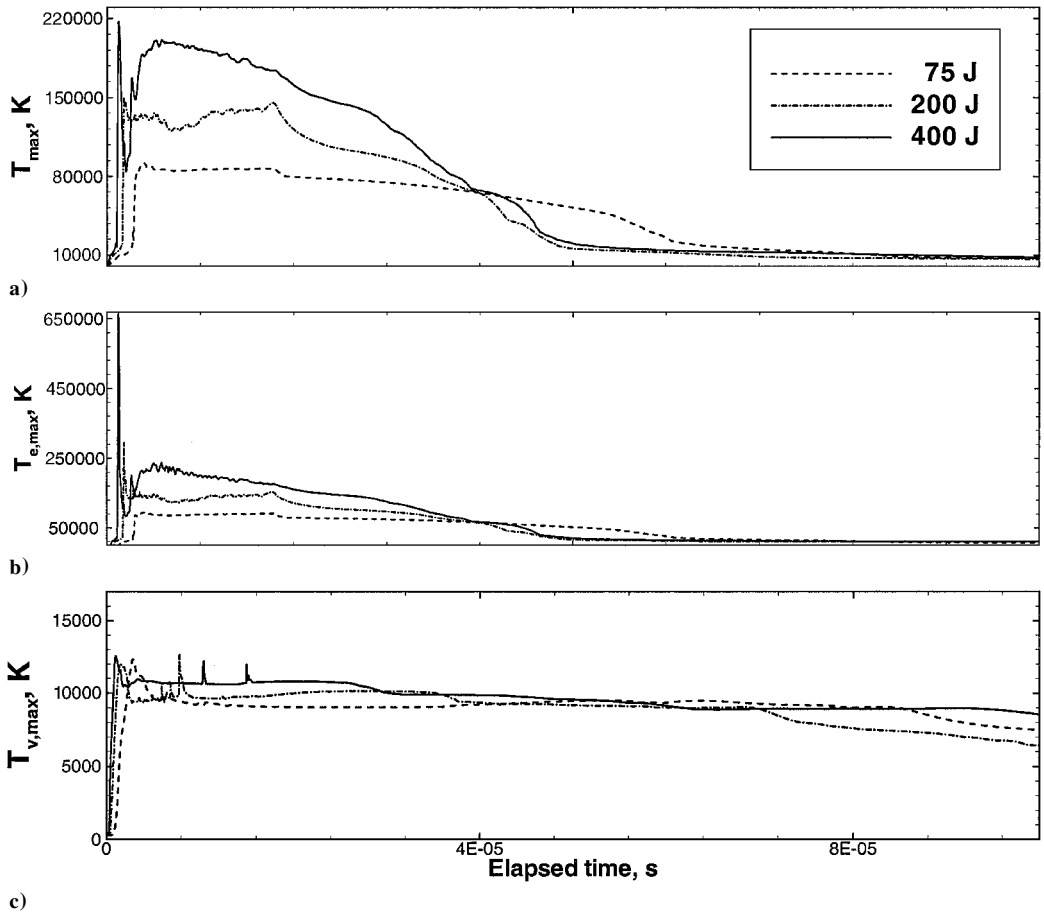

Fig. 5 Computed a) maximum gas temperature, b) electron temperature, and c) vibrational temperature histories for Model 200-3/4.

of the shock on the optical surface, and the convergence of the propagating shock at the tip. The higher the laser pulse energy, the earlier the rise and the higher the peak value. For the 400-J case, these three events occur at about 1, 18, and 100 μs, respectively. The maximum shock Mach number and pressure curves indicate that detonation occurs in all cases during the plasma ignition. The shock then strengthens again while impinging on the optical surface, and it strengthens for a third time while converging at the tip. The maximum electron number density curves show a third peak occurring at 100 μs for the 400-J case, corresponding to the maximum shown at the tip in Fig. 3. Note that none of the maximum electron number density peaks goes above the critical value, hence, the "opaque" condition never occurs for any of the cases computed. Note also that the shock speed is calculated as a function of the local pressure and ambient pressure ratio and levels off at sonic speed, hence, it is only meaningful when the shock Mach number is greater than unity. Figure 5 shows the computed maximum heavy gas temperature, electron temperature, and vibrational temperature histories. Again, the higher the laser pulse energy, the shorter the rise time and the higher the peak value. In terms of order of magnitude, the maximum electron temperature is very similar to that of the heavy gas temperature, whereas the maximum vibrational temperature is an order of magnitude lower.

The computational results indicate that a pulsed detonation wave takes place. The computed pressure contours at 10 μs in Fig. 6 indicate such a propagating detonation wave, still being maintained by the laser energy. The higher the pulse energy, the earlier the generation of a pulsed detonation wave. Part of this propagating detonation wave impinges on the parabolic optic and reflects off of the surface, as shown in the 18-μs pressure contours in Fig. 6. The reflected and nonreflected portions would combine to make a propagating Mach "ring." The body of revolution of the parabolic surface constitutes a hole in the middle of the Mach ring. The size of the hole decreases as the Mach ring propagates down the optic surface; eventually it reduces to zero as the shock reaches the tip. Note that the phenomenon of a propagating Mach ring on the optical surface is very similar to that of a propagating Mach disk inside a bell nozzle during the startup transient,[35,36] except there is no hole in the Mach disk. This is because the aerospike optic geometry is an "inside-out" version of that of a contoured bell nozzle.

As the shock wave moves past the end of the shroud, the minor part that is attached to the inner shroud starts to wrap around the outer shroud, also shown in the 18-μs pressure contours in Fig. 6. As the wraparound progresses, the entire shock wave grows like an expanding, deformed ellipsoid. A forebody attaching "leg" eventually develops, as shown in the 100-μs pressure contours in Fig. 6. Eventually, the leg leaves the nose, and the ellipsoid expands to infinity. While the minor part of the shock wave is wrapping around the shroud, the major propagating Mach ring that is attached to the aerospike surface continues to move down the optical surface, providing thrust. As it moves past the tip of the spike, the hole in the middle of the Mach ring disappears and a curved Mach disk emerges (as part of the ellipsoid) beneath the lightcraft.

Although the propulsion physics of the laser lightcraft is computed, note that the goal of performance modeling is to compute the impulse or coupling coefficient. The instantaneous impulse delivered to a lightcraft at time t is calculated through temporal force integrations:

$$I_t = \int_0^t \int p \, \mathrm{d}A \, \mathrm{d}t$$

Note that the control surfaces include the forebody, shroud, and parabolic optic, thus, enclosing the entire lightcraft. By definition, the instantaneous coupling coefficient is calculated as the instantaneous impulse divided by the laser pulse energy:

$$C_t = I_t / E$$

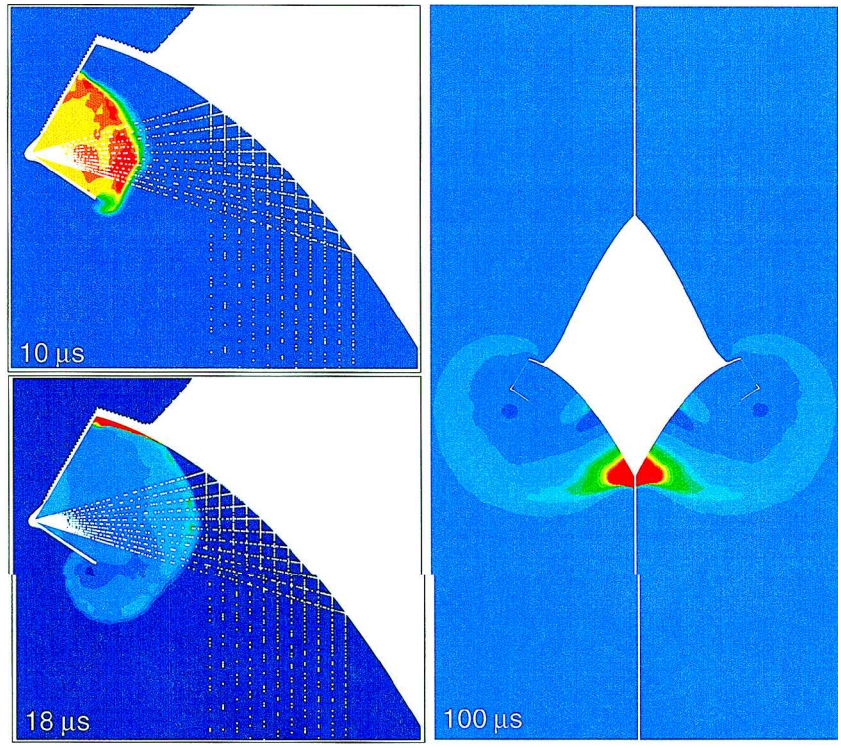

Fig. 6 Computed pressure contours for Model 200-3/4 pulsed by 400-J laser energy; contours color scale: 10 μs, 0.6–9.5, maximum 10; 18 μs, 4–15, maximum 51; and 100 μs 0.5–4, maximum 50.

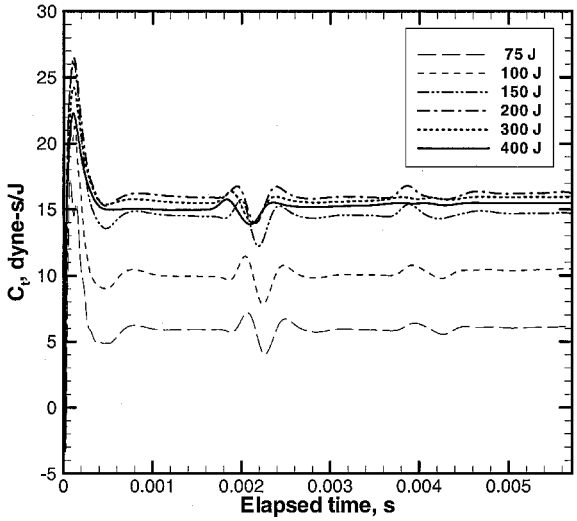

Fig. 7 Computed instantaneous coupling coefficient history for Model 200-3/4.

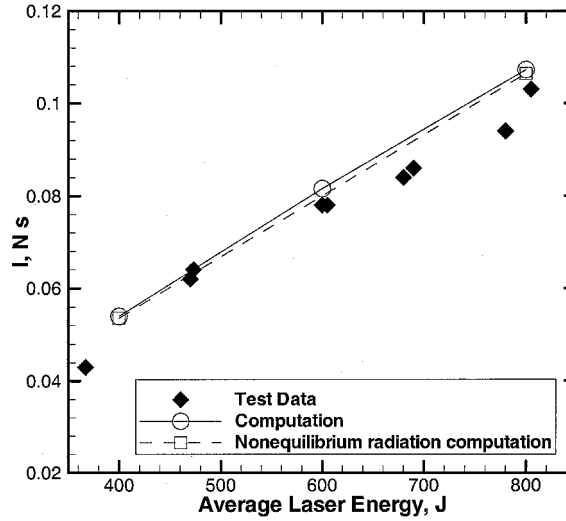

Fig. 8 Comparison of the impulses for Model A.

Figure 7 shows the computed instantaneous coupling coefficient history for Model 200-3/4. Peaks are reached at around 75–125 μs, about the time when the shock wave leaves the tip of the optical surface and the forebody attaching leg wraps past the shroud and touches the nose. The expanding shock wave creates a suction effect in the optical surface area and the forward-moving forebody-attaching shock generates a negative thrust. Although both effects decrease the impulse, and the instantaneous coupling coefficient drops, it is anticipated that both can be mitigated through design optimizations. The instantaneous coupling coefficient recovers somewhat once the forebody shock wave leaves the nose completely, as well as through air replenishment. Then it levels off, exhibiting slight oscillations due to the response to the transient flow environment. The highest peak value occurs for the 200-J laser pulse energy case. A traveling waveform occurs at about 2 ms, indicating the effect of the pressure wave reflected from the outer boundary. The effect of a second and weaker reflected wave occurs at around 4 ms.

It can be seen from Fig. 7 that the computed instantaneous coupling coefficient approaches an approximate steady state at an elapsed time of 5.7 ms. The final value of the instantaneous impulse or coupling coefficient at 5.7 ms is, therefore, used to compare with that of the measurement and is named as the impulse or coupling coefficient. The coupling coefficient is a performance measure unique to the pulsed laser propulsion and is conceptually similar to the specific impulse (generated thrust divided by propellant weight flow rate) of a chemical rocket.

Figure 8 shows a comparison of model-computed and experimentally measured impulses for Model A. The comparison is reasonably good, although it appears that the model prediction is slightly higher than that of the measurement. The nonequilibrium radiation computation made a slight improvement. Figure 9 shows a comparison

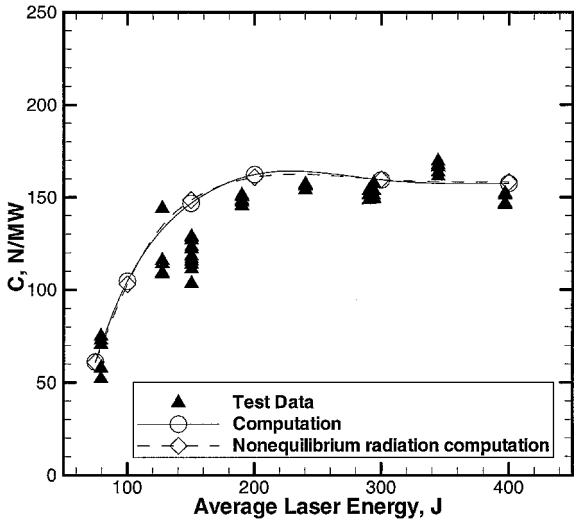

Fig. 9 Comparison of the coupling coefficients for Model 200-3/4.

of model-computed and experimentally measured coupling coefficients for Model 200-3/4. The measurement for Model 200-3/4 is, in general, much better than those for Model A, in terms of both quality and quantity. The model-computed coupling coefficients compare very well with those of the measurement, with a negligible edge going to the nonequilibrium radiation computation. The surprisingly small difference between the computed coupling coefficients with and without the nonequilibrium radiation is attributed to the small size and short duration of the hot plasma front. The scattering of the measured data is attributed mainly to the measurement of the laser energy, which varied from shot to shot (± 10 J) and for which an average over many pulses was used. Note that the slope of the impulse vs laser pulse energy plot in Fig. 8 is a coupling coefficient. In this case, the coupling coefficient for Model A is approximately a constant (126 N/MW) (Ref. 7) for laser energies ranging from 370 to 800 J.

In Fig. 9, it is shown that the coupling coefficient for Model 200-3/4 increases with laser pulse energies ranging from 75 to 200 J, then levels off at about 155 N/MW with laser pulse energies ranging from 200 to 400 J. These observations indicate that the coupling coefficient increases with laser pulse energy only at lower pulse energies. At higher pulse energies, the increase of laser pulse energy does not improve the level of coupling coefficient, although the impulse does increase with the laser pulse energy. It is speculated that the leveling off of coupling coefficient may be closely related to the limit of multiple ionization. That is, the increase of absorption of laser energy becomes marginal as the degree of multiple ionization increases. Another possibile cause is the shock losses. That is, the stronger the shock, the higher the energy losses. On the other hand, although both models are similar in size (hence, scaling is of minor consequence), the plateau coupling coefficient for Model 200-3/4 is higher than that for Model A. This is an encouraging observation because Model 200-3/4 is operated at a shorter pulse width than Model A is, indicating that there is potential for improving the laser lightcraft performance by packing in more laser energy in a shorter time.

Conclusions

A computational plasma aerodynamics model has been developed to study the propulsion physics of two experimental laser lightcrafts. The model development is based on a building-block approach, such that the model can be improved continuously with improved understanding of the physics. The model-computed laser propulsion physics, such as the optical breakdown and detonation wave propagation, agree well with those described in the literature. The model-computed coupling coefficient for a Model 200-3/4 laser lightcraft and the computed impulse for a Model A laser lightcraft agree reasonably well with those measured.

Acknowledgments

The authors wish to thank John Cole of Advanced Propulsion Research and Arthur Kirkindall of Propellantless Propulsion for supporting this study. The lead author wishes to thank Christopher Beairsto of the Directed Energy Team for the laser specifics, James Reilly of NorthEast Science and Technology, Shen Zhu of Science Directorate, and Jonathan Jones of the Propulsion Research Center for discussions on plasma resonance.

References

[1]Kantrowitz, A., "Propulsion to Orbit by Ground-Based Lasers," *Astronautics and Aeronautics*, Vol. 10, No. 5, 1972, pp. 74–76.

[2]Glumb, R. J., and Krier, H., "Concepts and Status of Laser-Supported Rocket Propulsion," *Journal of Spacecraft and Rockets*, Vol. 21, No. 1, 1984, pp. 70–79.

[3]Brandstein, A., and Levy, Y., "Laser Propulsion System for Space Vehicles," *Journal of Propulsion and Power*, Vol. 14, No. 2, 1998, pp. 261–269.

[4]Jeng, S.-M., and Keefer, D., "Theoretical Evaluation of Laser-Sustained Plasma Thruster Performance," *Journal of Propulsion*, Vol. 5, No. 5, 1989, pp. 577–581.

[5]Molvik, G. A., Choi, D., and Merkle, C. L., "Two-Dimensional Analysis of Laser Heat Addition in a Constant Absorptivity Gas," *AIAA Journal*, Vol. 23, No. 7, 1985, pp. 1053–1060.

[6]Myrabo, L., Raizer, Y. P., and Surzhikov, S. T., "Laser Combustion Waves in Laval Nozzles," *High Temperature*, Vol. 33, No. 1, 1995, pp. 11–20.

[7]Myrabo, L. N., Messitt, D. G., and Mead, F. B., Jr., "Ground and Flight Tests of a Laser Propelled Vehicle," AIAA Paper 98-1001, Jan. 1998.

[8]Mead, F. B., Jr., Myrabo, L. N., and Messitt, D. G., "Flight and Ground Tests of a Laser-Boosted Vehicle," AIAA Paper 98-3735, July 1998.

[9]Raizer, Y. P., "Subsonic Propagation of a Light Spark and Threshold Conditions for the Maintenance of Plasma by Radiation," *Soviet Physics—JETP*, Vol. 31, No. 6, 1970, pp. 1148–1154.

[10]Kemp, N. H., and Root, R. G., "Analytical Study of LSC Waves in Hydrogen," *Journal of Energy*, Vol. 3, No. 1, 1979, pp. 40–49.

[11]Gupta, R. N., Yos, J. M., Thompson, R. A., and Lee, K.-P., "A Review of Reaction Rates and Thermodynamic and Transport Properties for an 11-Species Air Model for Chemical and Thermal Nonequilibrium Calculations to 30,000 K," NASA RP-1232, 1990.

[12]Gordon, S., and McBride, B. J., "Computer Program for Calculation of Complex Chemical Equilibrium Compositions and Applications," NASA RP-1311, 1996.

[13]Nagulapally, M., Candler, G. V., Laux, C. O., and Kruger, C. H., "Numerical Simulation of a Constant Current Density Discharge in a Flowing Air Plasma," AIAA Paper 99-3477, June 1999.

[14]Barth, T. J., "Recent Developments in High Order *K*-Exact Reconstruction on Unstructured Meshes," AIAA Paper 93-0668, Jan. 1993.

[15]Fletcher, R., "Conjugate Gradient Methods for Indefinite Systems," *Lecture Notes in Mathematics*, Springer-Verlag, New York, Vol. 506, 1976, pp. 73–89.

[16]Saad, Y., and Schultz, M. H., "GMRES: A Generalized Minimal Residual Algorithm for Solving Nonsymmetric Linear Systems," *SIAM Journal of Scientific and Statistical Computing*, Vol. 7, No. 3, 1986, pp. 856–869.

[17]Landau, L., and Teller, E., "Zur Theorie der Schalldispersion," *Physikalische Zeitschrift der Soviet Union*, Vol. 10, No. 34, 1936, pp. 34–43.

[18]Gnoffo, P. A., Gupta, R. N., and Shinn, J. L., "Conservation Equations and Physical Models for Hypersonic Air Flows in Thermal and Chemical Non-equilibrium," NASA TP 2867, 1989.

[19]Park, C., "Review of Chemical–Kinetic Problems of Future NASA Missions, I: Earth Entries," *Journal of Thermophysics and Heat Transfer*, Vol. 7, No. 3, 1993, pp. 385–398.

[20]Mertogul, A.E., "Modeling and Experimental Measurements of Laser Sustained Hydrogen Plasmas," Ph.D. Dissertation, Dept. of Mechanical Engineering, Univ. of Illinois at Urbana–Champaign, Urbana, IL, Feb. 1993.

[21]Edwards, A. L., and Fleck, J. A., Jr., "Two-Dimensional Modeling of Aerosol-Induced Breakdown," *Journal of Applied Physics*, Vol. 50, No. 6, 1979, pp. 4307–4313.

[22]Modest, M. F., *Radiative Heat Transfer*, McGraw–Hill, New York, 1993, pp. 54, 55.

[23]Raizer, Y. P., and Tybulewicz, A., *Laser-Induced Discharge Phenomena*, Studies in Soviet Science, edited by G. C. Vlases and Z. A. Pietrzyk, Consultants Bureau, New York, 1977, pp. 242, 243.

[24]Zel'dovich, Y. B., and Raizer, Y. P., *Physics of Shock Waves and High Temperature Hydrodynamic Phenomena*, Vol. 1, edited by W. D. Hayes and R. F. Probstein, Academic Press, New York, 1966, pp. 277–281.

[25]Hartung, L., "Theory and User's Manual for Loran Code," NASA TM-4564, 1994.

[26]Gogel, T. H., Duouis, M., and Messerschmid, E. W., "Radiation Transport Calculation in High-Enthalpy Environment for Two-Dimensional Axisymmetric Geometries," *Journal of Thermophysics and Heat Transfer*, Vol. 8, No. 4, 1994, pp. 744–750.

[27]Hartung, L. C., and Hassan, H. A., "Radiation Transport Around Axisymmetric Blunt Body Vehicles Using a Modified Differential Approximation," *Journal of Thermophysics and Heat Transfer*, Vol. 7, No. 2, 1993, pp. 220–227.

[28]Surzhikov, S. T., "Calculation of the Radiation Flux Divergence near the Region of Local Heat Release by Quadromoment Method," *Proceedings of the First International Symposium on Radiation Transfer*, Begell House, New York, 1995, pp. 92–106.

[29]Liu, J., Shang, H., Chen, Y.-S., and Wang, T.-S., "Analysis of Discrete Ordinates Method with Even Parity Formulation," *Journal of Thermophysis and Heat Transfer*, Vol. 11, No. 2, 1997, pp. 253–260.

[30]Coelho, P. J., and Carvalho, M. G., "A Conservative Formulation of the Discrete Transfer Method," *Journal of Heat Transfer*, Vol. 119, No. 1, 1997, pp. 118–128.

[31]Brown, S. C., *Basic Data of Plasma Physics*, Technology Press of the Massachusetts Institute of Technology and Wiley, New York, 1959, pp. 308, 309.

[32]Hora, H., *Laser Plasmas and Nuclear Energy*, Plenum, New York, 1975, pp. 24–26.

[33]Lyons, P. W., Myrabo, L. N., Jones, R. A., Nagamatsu, H. T., and Manka, C., "Experimental Investigation of a Unique Airbreathing Pulsed Laser Propulsion Concept," AIAA Paper 91-1922, June 1991.

[34]Fouts, C., Steinbrenner, J., and Chawner, J., "CFD Meshing in Collaborative and Customized Environments," AIAA Paper 2002-0751, Jan. 2002.

[35]Wang, T.-S., "Numerical Study of the Transient Nozzle Flow Separation of Liquid Rocket Engines," *Computational Fluid Dynamics Journal*, Vol. 1, No. 3, 1992, pp. 319–328.

[36]Wang, T.-S., and Chen Y.-S., "Unified Navier–Stokes Flowfield and Performance Analysis of Liquid Rocket Engines," *Journal of Propulsion and Power*, Vol. 9, No. 5, 1993, pp. 678–685.